



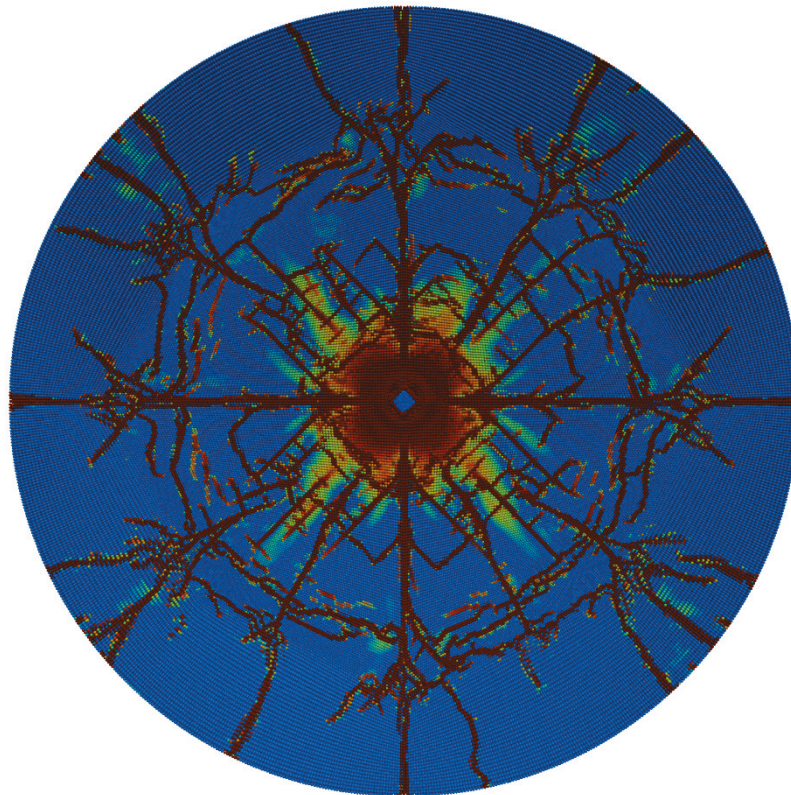
**US Army Corps
of Engineers®**
Engineer Research and
Development Center



A Multiscale Meshfree Approach to Modeling Damage of Cor-Tuf without Fibers Using Fracture Energy Experiments

Jesse A. Sherburn, William F. Heard, Brett A. Williams,
and Paul A. Sparks

April 2019



The U.S. Army Engineer Research and Development Center (ERDC) solves the nation's toughest engineering and environmental challenges. ERDC develops innovative solutions in civil and military engineering, geospatial sciences, water resources, and environmental sciences for the Army, the Department of Defense, civilian agencies, and our nation's public good. Find out more at www.erdclibrary.usace.army.mil.

To search for other technical reports published by ERDC, visit the ERDC online library at <http://acwc.sdp.sirsi.net/client/default>.

A Multiscale Meshfree Approach to Modeling Damage of Cor-Tuf without Fibers Using Fracture Energy Experiments

Jesse A. Sherburn, William F. Heard, Brett A. Williams, and Paul A. Sparks

*Geotechnical and Structures Laboratory
U.S. Army Engineer Research and Development Center
3909 Halls Ferry Road
Vicksburg, MS 39180-6199*

Final report

Approved for public release; distribution is unlimited.

Prepared for U.S. Army Engineer Research and Development Center
3909 Halls Ferry Road
Vicksburg, MS 39180-6199

Under Program element number 61102

Abstract

Many continuum damage mechanics models for cementitious materials are typically phenomenological in design. Recent work has shown that a physics-based multiscale approach to modeling damage is efficient and effective. In order to use a multiscale approach, appropriate experimental data are necessary to model the microscale calculations that will then inform the continuum-scale calculations. This work uses the multiscale approach and experimentally determines the parameters necessary to model the microscale calculations. Notched three-point beam experiments were performed to determine the fracture energy of the ultra-high performance concrete known as Cor-Tuf. The fracture energy is then used by a simplified microscale calculation to determine a physics-based damage evolution equation that can be used in continuum-scale calculations. A meshfree method is used to show the usefulness of the newly determined damage evolution equation. Both a quasi-static application and a dynamic application are shown as examples.

DISCLAIMER: The contents of this report are not to be used for advertising, publication, or promotional purposes. Citation of trade names does not constitute an official endorsement or approval of the use of such commercial products. All product names and trademarks cited are the property of their respective owners. The findings of this report are not to be construed as an official Department of the Army position unless so designated by other authorized documents.

DESTROY THIS REPORT WHEN NO LONGER NEEDED. DO NOT RETURN IT TO THE ORIGINATOR.

Contents

Abstract	ii
Figures and Tables.....	iv
Preface.....	v
1 Introduction.....	1
1.1 Background.....	1
1.2 Objectives.....	2
1.3 Scope	2
2 Meshfree Multiscale Framework.....	3
2.1 Macroscale RKPM	3
2.2 Microscale RKPM	5
2.3 Energy-bridging homogenization	6
3 Fracture Energy Experiments	8
4 Numerical Calculations	12
4.1 Microscale calculation.....	12
4.2 Macroscale calculation	14
4.3 Ballistic numerical application.....	21
5 Conclusions.....	28
References	29
Report Documentation Page	

Figures and Tables

Figures

Figure 1. Energy-bridging homogenization from the microscale to macroscale.	7
Figure 2. Test configuration for three-point bending.	9
Figure 3. Experimental setup of the three-point bending test.	9
Figure 4. DIC strain field data for XX-strain (horizontal) showing location of crack path.	10
Figure 5. Load versus CMOD for the SENB experiments.	11
Figure 6. Microcell loading conditions.	12
Figure 7. Cohesive law implemented in NMAP-Micro.	13
Figure 8. Damage evolution curve based on the single-crack microscale calculation.	14
Figure 9. Three-point bending simulation setup.	15
Figure 10. AFC hydrostatic fit for Cor-Tuf used in this study.	16
Figure 11. AFC failure surface fit for Cor-Tuf used in this study.	18
Figure 12. Experimental results compared to NMAP calculation.	19
Figure 13. Damage field results of the NMAP MIDM three-point beam type A calculation.	20
Figure 14. MIDM AFC NMAP calculations versus original AFC NMAP calculations.	20
Figure 15. X-ray computed micro-tomography image of Cor-Tuf.	21
Figure 16. Setup of numerical ballistic perforation experiment.	22
Figure 17. Strain rate adjusted damage evolution law for two different strain rates.	23
Figure 18. Residual velocity results of NMAP perforation calculations.	24
Figure 19. Damage field contours of the 500 m/s NMAP perforation calculation with MIDM improvements (impact face, back face, and side view).	25
Figure 20. Damage field contours of the 500-m/s NMAP perforation calculation with original AFC model (impact face, back face, and side view).	26

Tables

Table 1. Nominal Cor-Tuf beam dimensions.	9
Table 2. Fracture energy for beam types A, B, and C.	11
Table 3. Cohesive law parameters for microcell calculations.	13
Table 4. AFC constants used for Cor-Tuf.	18

Preface

This study was conducted under the Military Engineering Basic Research Program sponsored by the Assistant Secretary of the Army for Acquisition, Logistics, and Technology under PE 61102, Project T22 "Material Modeling for Force Protection," Task 02. The technical monitor was Ms. Pamela G. Kinnebrew.

This work was performed by the Survivability Engineering Branch (GSV) of the Geosciences and Structures Division (GS) and the Concrete and Materials Branch (GMC) of the Engineering Systems and Materials Division (GM), U.S. Army Engineer Research and Development Center, Geotechnical and Structures Laboratory (ERDC-GSL).

At the time of publication, Mr. Omar G. Flores was Chief, CEERD-GSV; Mr. Christopher M. Moore was Chief, CEERD-GMC; Mr. James L. Davis was Chief, CEERD-GS; Mr. Jeffrey G. Averett was Acting Chief, CEERD-GM; and Ms. Pamela G. Kinnebrew, CEERD-GZT, was Technical Director for Survivability and Protective Structures. The Deputy Director of ERDC-GSL was Mr. Charles W. Ertle II, and the Director was Mr. Bartley P. Durst.

COL Ivan P. Beckman was the Commander of ERDC, and Dr. David W. Pittman was the Director.

Unit Conversion Factors

Multiply	By	To Obtain
feet	0.3048	meters
inches	0.0254	meters
pounds (force) per square inch	6.894757	kilopascals
pounds (mass)	0.45359237	kilograms

1 Introduction

1.1 Background

Damage mechanics has been a suitable approach for predicting the behavior of quasi-static and high-strain-rate loading conditions for more than half a century. The theory of continuum damage mechanics (CDM) was first proposed by Kachanov (1958) and Rabotnov (1969) to creep problems. The approach was developed to describe the materials' progressive deterioration of microdefects from a state of being undamaged (virgin state) to a state of crack growth and propagation at the macroscopic continuum level. The crack is idealized by a band of damaged material at the continuum level, and microcracks and voids are modeled at the microscale.

Damage evolution within a multi-scale computational framework has been used to address these issues of microstructural resolution and computational efficiency. Recent efforts have led to a host of numerical investigations in which micromechanical models exploit homogenization techniques to link the representative volume element with the macrostructural continuum model. Lee et al. (1999) and Jain and Ghosh (2009) used Voronoi cell finite elements to explicitly model the microstructure and asymptotically expand the boundary-valued problem. Oskay and Fish (2007) developed a nonlocal eigendeformation homogenization method based on two-scale asymptotic expansion to describe damage in the composite structures. To reduce the computational cost due to solving a system of nonlinear equations, Sparks and Oskay (2016) proposed the method of overlapping failure paths. Ren et al. (2011) used enriched reproducing kernel particle methods (RKPMs) to investigate microcracks informed damage models (MIDMs). The damage evolution law is obtained from Helmholtz free energy from the microcrack and the continuum. This energy-bridging method is based on fracture mechanics and exploits the evolution of the microstructural strain field as the driver of the damage evolution function. A plethora of the CDM homogenization models has been applied to various materials and employed to solve a wide variety of problems, but the focus was on employing numerical experiments to validate the aforementioned computational methods.

Other efforts in the literature have been devoted to characterizing the damage evolution function by utilizing an arc tangent damage evolution function based on material parameters (Oskay and Fish 2007; Sparks and

Oskay 2016). Such efforts provide reasonable approximations to describe the damage evolution at the microscopic and continuum levels, and the reliability of the approach is dependent on fitting the material parameters to experiments. The present work aims to extend the works of Ren et al. (2011) and Sherburn et al. (2015) by presenting the development of a damage evolution model that is directly informed by experiments that characterize the ultra-high performance concrete (UHPC) known as Cor-Tuf. The experiments investigate UHPC fracture energy of three different-sized, single-edge notched beams (SENBs) in closed-loop three-point tests. The crack evolution microcell model employs the experimental parameters, and numerical simulations are modeled to derive the corresponding damage evolution function in the continuum level.

The strength of the MIDM in this work lies in the coupling of the UHPC experimental data to determine the physical parameters necessary to perform the microscale calculations. The previous work by Ren et al. (2011) relied on data found in the literature. This work will complete both the experimental characterization and the microscale numerical portion to determine an appropriate macroscale damage evolution function that will be used in macroscale numerical calculations of the experimental testing.

1.2 Objectives

There are two main objectives for this report. The first objective is to experimentally measure the fracture energy of Cor-Tuf without fibers by using standard beam experiments designed to measure fracture energy. The second objective is to use the experimentally measured value of fracture energy as input for running microscale single-crack calculations. These microscale calculations will be used to develop a macroscale damage evolution function that will be implemented and demonstrated in a few macroscale scenarios.

1.3 Scope

The organization of this report will be the following: The macroscale RKPM, microscale RKPM, and energy-bridging homogenization framework will be described in Chapter 2. In Chapter 3, the experimental approach, techniques, and data used in the multiscale modeling study are presented. In Chapter 4, the microscale and macroscale calculation results are presented alongside the experimental data along with a set of ballistic perforation calculations. Chapter 5 will make concluding remarks.

2 Meshfree Multiscale Framework

2.1 Macroscale RKPM

The RKPM framework's ability to accurately model large deformation without the complexities of mesh-distortion problems makes the methodology extremely attractive for solving problems involving impact and penetration of brittle materials. The RKPM framework approximates the solution of the partial differential equation by utilizing a point-based discretization. The meshfree shape functions are constructed by using overlapping kernels of compact support. The benefits of the RKPM framework are the following: (1) the constraint of the geometric conformity on the domain discretization relaxes, (2) employing a Lagrangian discretization leads to the attainment of clear material interfaces, and (3) the formulation has consistency as opposed to smooth particle hydrodynamics (SPH), which lacks that attribute (Belytschko et al. 1998).

This section will briefly cover the RKPM approximation method. Consider a heterogeneous closed domain, $\bar{\Omega} = \Omega \cup d\Omega$, where Ω is the open domain and $d\Omega$ is the boundary of Ω . Spatially, the RKPM formulation uses a discrete kernel approximation (Chen et al. 1996) with reference to material coordinates, \mathbf{X} , to approximate the displacements, $\mathbf{u}(\mathbf{X}, t)$, as

$$\mathbf{u}^h(\mathbf{X}, t) = \sum_{I \in N} \Psi_I(\mathbf{X}) \mathbf{d}_I(t), \quad (1)$$

where \mathbf{u}^h is the approximation of $\mathbf{u}(\mathbf{X}, t)$ and $\mathbf{d}_I(t)$ are unknown coefficients of the RK approximation that are to be solved for in the meshfree solution. $\Psi_I(\mathbf{X})$ is the RK shape function referenced to the I^{th} node, and N is the number of nodes. The RK shape function is modified and constructed as a correction of the compact kernel function:

$$\begin{aligned} & \phi_a(\mathbf{X} - \mathbf{X}_I) \\ \Psi_I(\mathbf{X}) &= C(\mathbf{X}; \mathbf{X} - \mathbf{X}_I) \phi_a(\mathbf{X} - \mathbf{X}_I) \end{aligned} \quad (2)$$

where continuity and locality are inherited from the kernel function. The correction function, $C(\mathbf{X}; \mathbf{X} - \mathbf{X}_I)$, enforces the reproducibility conditions of the basis. A novel feature of RKPM is that any arbitrary basis can be reproduced due to the enforcement of the reproducing condition.

Employing a set of n^{th} order complete monomials, the correction function is denoted as

$$C(\mathbf{X}; \mathbf{X} - \mathbf{X}_I) = \sum_{|\alpha|=0}^n (\mathbf{X} - \mathbf{X}_I)^\alpha b_\alpha(\mathbf{X}) = \mathbf{H}^T(\mathbf{X} - \mathbf{X}_I) \mathbf{b}(\mathbf{X}), \quad (3)$$

where $|\alpha| \equiv \alpha_1 + \alpha_2 + \alpha_3$, $(\mathbf{X} - \mathbf{X}_I)^\alpha \equiv (X_1 - X_{1I})^{\alpha_1} (X_2 - X_{2I})^{\alpha_2} (X_3 - X_{3I})^{\alpha_3}$, and $b_\alpha(\mathbf{X}) \equiv b_{\alpha_1 \alpha_2 \alpha_3}(\mathbf{X})$. The n^{th} order complete basis functions are contained in $\mathbf{H}^T(\mathbf{X} - \mathbf{X}_I)$, where

$$\mathbf{H}^T(\mathbf{X} - \mathbf{X}_I) = [1, (X_1 - X_{1I}), (X_2 - X_{2I}), (X_3 - X_{3I}), (X_1 - X_{1I})^2, \dots, (X_3 - X_{3I})^n]. \quad (4)$$

The reproducing conditions

$$\begin{aligned} \sum_{I \in N} \Psi_I(\mathbf{X}) \mathbf{X}_I^\alpha &= \mathbf{X}^\alpha \\ |\alpha| &= 0, 1, \dots, n \end{aligned} \quad (5)$$

are used to obtain the vector of coefficients, $\mathbf{b}(\mathbf{X}) = \mathbf{M}^{-1}(\mathbf{X}) \mathbf{H}(0)$, where $\mathbf{H}^T(0) = [1, 0, \dots, 0]$, and $\mathbf{M}(\mathbf{X})$ is a moment matrix

$$\mathbf{M}(\mathbf{X}) = \sum_{I \in N} \mathbf{H}(\mathbf{X} - \mathbf{X}_I) \mathbf{H}^T(\mathbf{X} - \mathbf{X}_I) \phi_a(\mathbf{X} - \mathbf{X}_I) \quad (6)$$

Consequently, the Lagrangian RK shape function is

$$\Psi_I(\mathbf{X}) = \mathbf{H}^T(\mathbf{X} - \mathbf{X}_I) \mathbf{M}^{-1}(\mathbf{X}) \mathbf{H}(0) \phi_a(\mathbf{X} - \mathbf{X}_I) \quad (7)$$

The numerical integration technique used in this study is the stabilized conforming nodal integration (SCNI; Chen et al. 2001). SCNI is appropriate for applications that involve large deformations but do not fracture. To explain SCNI, first consider the Galerkin weak form of the equation of motion

$$\begin{aligned} \int_{\Omega} \rho \mathbf{w}^h \cdot \dot{\mathbf{u}}^h d\Omega + \int_{\Omega} \boldsymbol{\varepsilon}(\mathbf{w}^h) : \boldsymbol{\sigma}(\boldsymbol{\varepsilon}(\mathbf{u}^h)) d\Omega \\ - \int_{\Omega} \mathbf{w}^h \cdot \mathbf{b} d\Omega - \int_{\Gamma^h} \mathbf{w}^h \cdot \mathbf{t} d\Gamma = 0, \end{aligned} \quad (8)$$

where ρ is density, \mathbf{w}^h and \mathbf{u}^h are test and trial functions, $\boldsymbol{\varepsilon}$ is strain, $\boldsymbol{\sigma}$ is stress, Γ^h is the natural boundary, and \mathbf{b} and \mathbf{t} are body forces and surface tractions, respectively. Gradients are approximated through a gradient-smoothing operator

$$\tilde{\boldsymbol{\epsilon}}_I(\mathbf{u}^h) = (1/V_I) \int_{\partial\Omega_I} (1/2)(\mathbf{u}^h \otimes \mathbf{n} + \mathbf{n} \otimes \mathbf{u}^h) d\Gamma, \quad (9)$$

where $\partial\Omega_I$ is the boundary of an integration subdomain Ω_I corresponding to the I^{th} node, \mathbf{n} is the outward normal to the cell boundary, V_I is the strain-smoothing cell volume, and $\tilde{\boldsymbol{\epsilon}}_I$ is the smoothed nodal strain. A further discussion of Eq. (9) can be found in Guan et al. (2011). The advantage of using the gradient-smoothed operator is that the derivatives of \mathbf{u} are no longer required to be calculated. Only the conforming cell topological features such as the boundary surface area, outward normal, and the boundary segment midpoint location are required to construct the strain approximation. This leads to an efficient calculation of strain, and an optimal convergence rate is achieved.

2.2 Microscale RKPM

For the microscale calculations, an extrinsically enriched RKPM formulation is introduced following the work of Lin et al. (2016) and Ren et al. (2011) in order to properly model discontinuities. A brief summary of this enriched RKPM will be described here. The enriched near-tip displacement field is described by

$$\mathbf{u}^h(\mathbf{X}, t) = \sum_{I \in N} \Psi_I(\mathbf{X}) d_I(t) + \sum_{J \in N_{cut}} H(\mathbf{X}) \Psi_J(\mathbf{X}) a_J(t) + \sum_{K \in N_{tip,i}} f_i(\mathbf{X}) \Psi_K(\mathbf{X}) b_K(t), \quad (10)$$

where N_{cut} is the number of the enriched nodes cut by the discontinuity, and N_{tip} is the number of enriched nodes near the tip of the discontinuity. The enrichment function $H(\mathbf{X})$ is defined as

$$H(\mathbf{X}) = \begin{cases} 1 & y > 0 \\ -1 & y < 0 \end{cases} \quad (11)$$

where y is the local coordinate system normal to the discontinuity surface. The singular-tip enrichment functions, $f_i(\mathbf{X})$, are the following:

$$f_i(\mathbf{X}) = \mathbf{f}(r, \theta) = \left\{ \sqrt{r} \sin\left(\frac{\theta}{2}\right), \sqrt{r} \cos\left(\frac{\theta}{2}\right), \sqrt{r} \sin\left(\frac{3\theta}{2}\right), \text{and } \sqrt{r} \cos\left(\frac{3\theta}{2}\right) \right\}. \quad (12)$$

In a similar fashion the cohesive zone model enrichment functions are defined as

$$f_i(\mathbf{X}) = \mathbf{f}(r, \theta) = \left\{ r \sin\left(\frac{\theta}{2}\right), r^{\frac{3}{2}} \sin\left(\frac{\theta}{2}\right), r^2 \sin\left(\frac{\theta}{2}\right) \right\}, \quad (13)$$

where θ is the angle between a local x-axis relative to the discontinuity and the connected line of the crack tip and the enriched node, and r is the radius to the evaluation point. For a thorough explanation, see Lin (2014). The integration method used in this process is SCNI-based and is described in the enhanced RKPM context in Lin (2014).

2.3 Energy-bridging homogenization

The methodology for the MIDM employs principles based on the thermodynamics of cracked microstructure and the corresponding damaged macroscopic continua. Ren et al. (2011) introduced the relationship between the microcracks due to material deterioration at the local microscopic level and the damaged continuum. Figure 1 shows the energy-based bridging between multiple scales. The representative microcell has heterogeneities and defects within the domain of the microstructure, Ω_y , and the stresses and strains are obtained through homogenization. The Helmholtz free energy (HFE) of the cracked microcell, Ψ^ε , is defined as

$$\Psi^\varepsilon = \frac{1}{2} \boldsymbol{\sigma}^\varepsilon : \boldsymbol{e}^\varepsilon \quad (14)$$

where $\boldsymbol{\sigma}^\varepsilon$ and $\boldsymbol{e}^\varepsilon$ are the microcell stress and strain, respectively. The homogenized macroscale HFE is obtained through volume-averaging the microcell HFE and the respective microcell displacement field, \mathbf{u}^ε , over the domain of the microstructure, Ω_y :

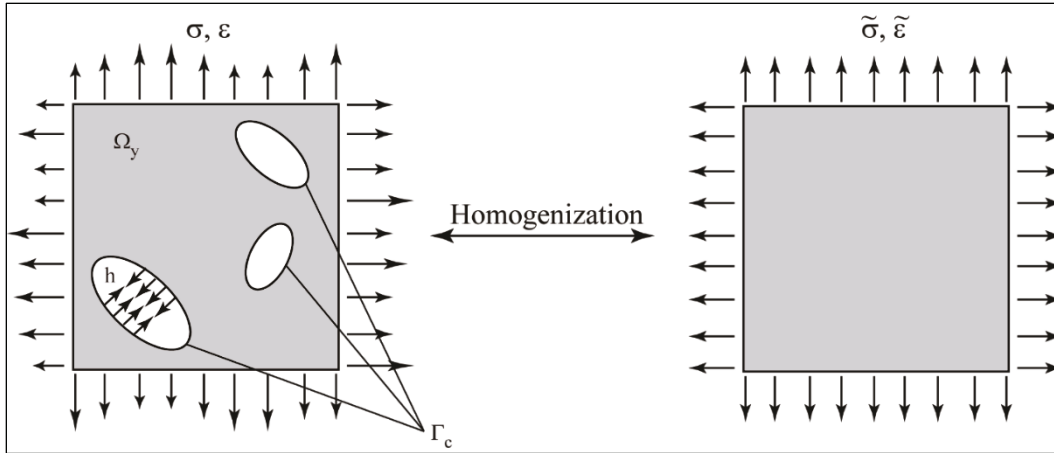
$$\bar{\Psi} = \frac{1}{V_y} \left(\int_{\Omega_y} \Psi^\varepsilon d\Omega + \frac{1}{2} \int_{\Gamma_c} \mathbf{u}^\varepsilon \cdot \mathbf{h} d\Gamma \right) , \quad (15)$$

where V_y is the microcell volume. From Eq. (15), the opening displacements corresponding to the microcracks are modelled explicitly, and it is straightforward to see the homogenized HFE is a function of the microcell stresses and strains. The microcell fracture is related to the macroscopic HFE by a two-scalar continuum damage model expressed as

$$\bar{\Psi} = (1 - d^+) \Psi_0^+ + (1 - d^-) \Psi_0^- , \quad (16)$$

where d^+ and d^- are the damage parameters tension and shear, respectively, and Ψ_0 is the free energy corresponding with the undamaged continuum. The subsequent HFE terms are defined according to signs of the eigenvalues in the principal stress.

Figure 1. Energy-bridging homogenization from the microscale to macroscale.



The Clausius-Duhem inequality of irreversible thermodynamics derived from Eq. 16 is stated as

$$\Psi_0^\pm = Y^\pm \quad , \quad (17)$$

where Y^\pm are the damage energy release rates. Combining Eqs. (16-17), the microscale-informed tensile damage evolution law is obtained as

$$d^+ = 1 - \frac{\partial \Psi}{\partial Y^+} \approx 1 - \frac{\Delta \Psi}{\Delta Y^+} \quad (18)$$

and can be evaluated by using a finite difference method. A fully tensorial damage model can be obtained from incorporating the damage evolution law into the macroscale equations. For brevity, a summary of the key features of the MIDM was discussed; for further explanation refer to Ren et al. (2011).

3 Fracture Energy Experiments

The microscale calculations utilized experimental data captured through a series of three-point bend tests conducted on UHPC single-edge notched beams (SENB). The SENB test series was designed to capture the fracture energy of the UHPC. Three different beam sizes were selected based on previous work by O'Neil (2008). O'Neil measured the fracture toughness and fracture energy of an early variant of this ERDC-developed UHPC through a two-parameter fracture model (Jenq and Shah 1985) and a numerical method created by Navalurkar et al. (1999). Since the work of O'Neil, the UHPC has been further developed, modified, and patented by the ERDC. Subsequently, Williams et al. (2009) published the updated UHPC mixture proportions with casting and curing guidelines, and laboratory quasi-static triaxial characterization data. This updated ERDC UHPC, known as Cor-Tuf, is the material used in this study.

Table 1 reports the nominal dimensions for the three different beam sizes investigated, while Figure 2 and Figure 3 show the test setup for the fracture energy experiments. The notched beams were center-loaded with supports at each beam end. Supports were designed to minimize friction, with one support allowing rotation about an axis parallel to the beam's longitudinal axis to alleviate potential torsion in the beam. An MTS servo-hydraulic testing machine was used to load the beams in a closed-loop control mode with a crack mouth opening displacement (CMOD) clip-on gauge as the feedback signal. The CMOD gauge was clipped to epoxy-mounted knife edges, as shown schematically in Figure 2. The CMOD displacement rate was $0.0005 \times (\text{beam depth})$ per min for all experiments. In addition to the CMOD gauge, surface strains and crack growth were measured by using 3-D digital image correlation (DIC). DIC is an experimental technique using calibrated digital cameras to capture specimen surface displacement/deformation and an algorithm to calculate the associated surface strains. For this test series, calibrated stereo digital cameras with a pixel resolution of $64 \mu\text{m}$ were used to capture movement of the specimen surface in 3-D space under load. This technique helped to monitor beam response and ensure proper loading conditions applied by the loading apparatus. A comprehensive overview of the 3D DIC theory and a description of the experimental technique is covered by Sutton et al. (2009).

Table 1. Nominal Cor-Tuf beam dimensions.

Beam Type	Length (l) (mm)	Width (w) (mm)	Depth (d) (mm)	Notch Length (a_0/d)	Notch Width (mm)	Number of Beams
A	171	38	38	0.33	3	7
B	343	38	76	0.33	3	6
C	513	38	114	0.33	3	2

Figure 2. Test configuration for three-point bending.

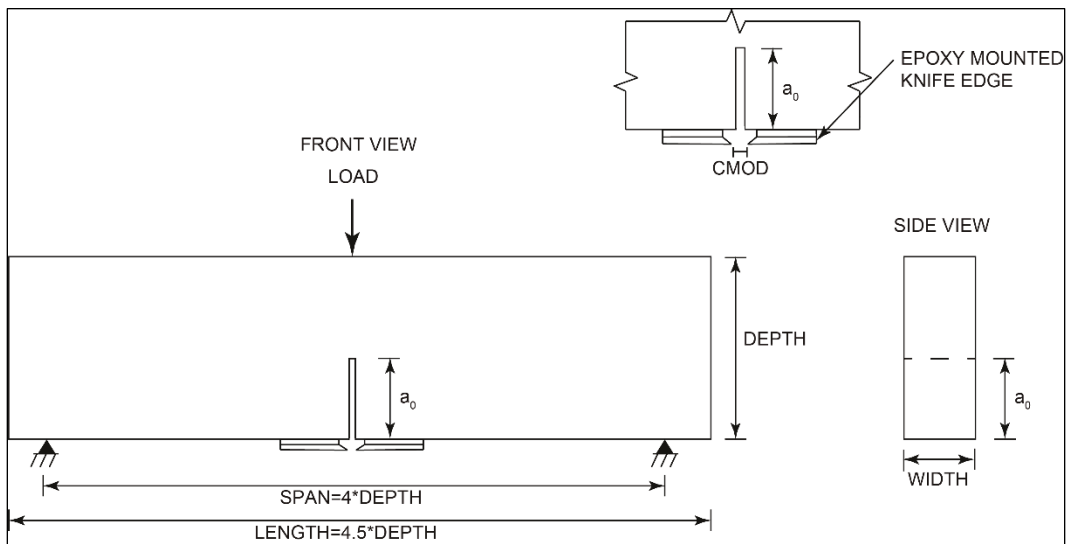
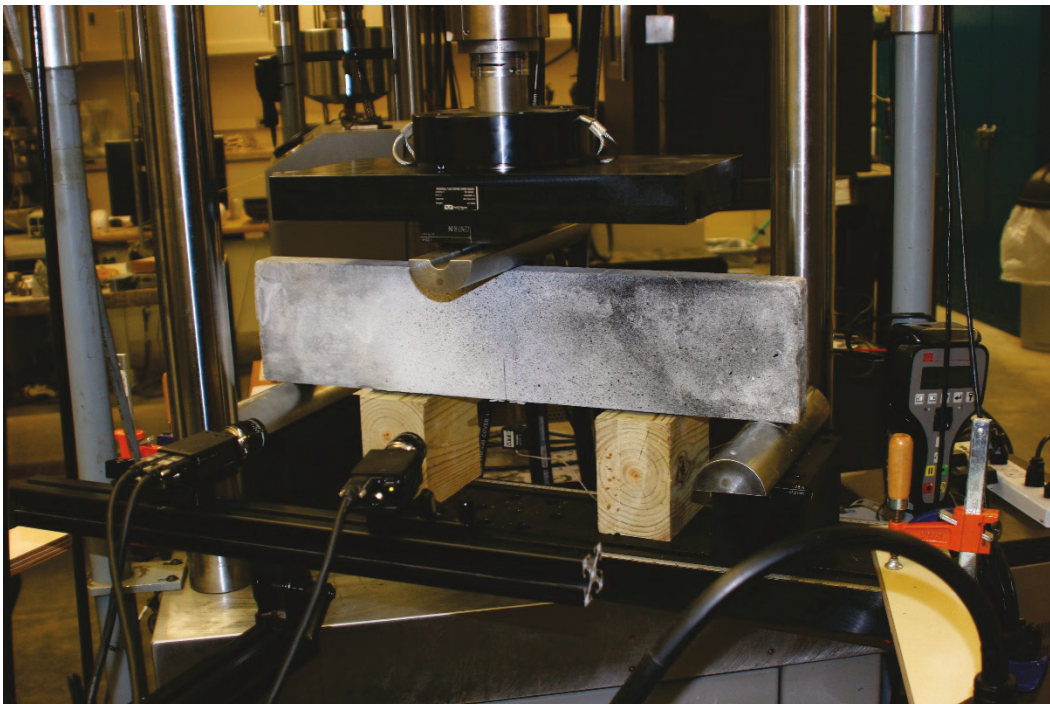


Figure 3. Experimental setup of the three-point bending test.



Upon completion of the SENB test series, the 3D DIC strain field data were analyzed as a qualitative check for proper loading conditions. As an example, Figure 4 shows the strain field in the XX direction (i.e., horizontal, axis parallel with beam length) for beam type C, test number 1. The YY and ZZ strain field data were also evaluated to ensure near-ideal loading conditions were achieved in each test. Results from all of the SENB experiments are shown in Figure 5. Figure 5 is a plot of the load versus CMOD data obtained for all three beam sizes. The fracture energy was calculated by using the area under the load-CMOD curves and the beam ligament area of each respective beam. These values are reported in Table 2.

Figure 4. DIC strain field data for XX-strain (horizontal) showing location of crack path.

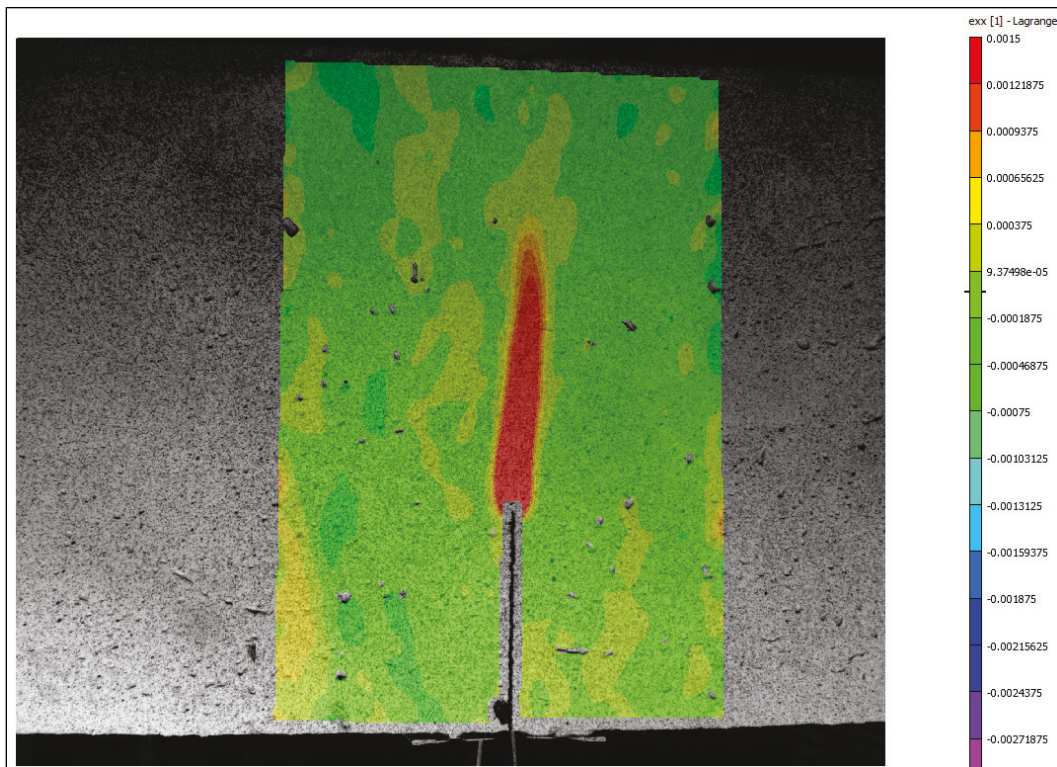


Figure 5. Load versus CMOD for the SENB experiments.

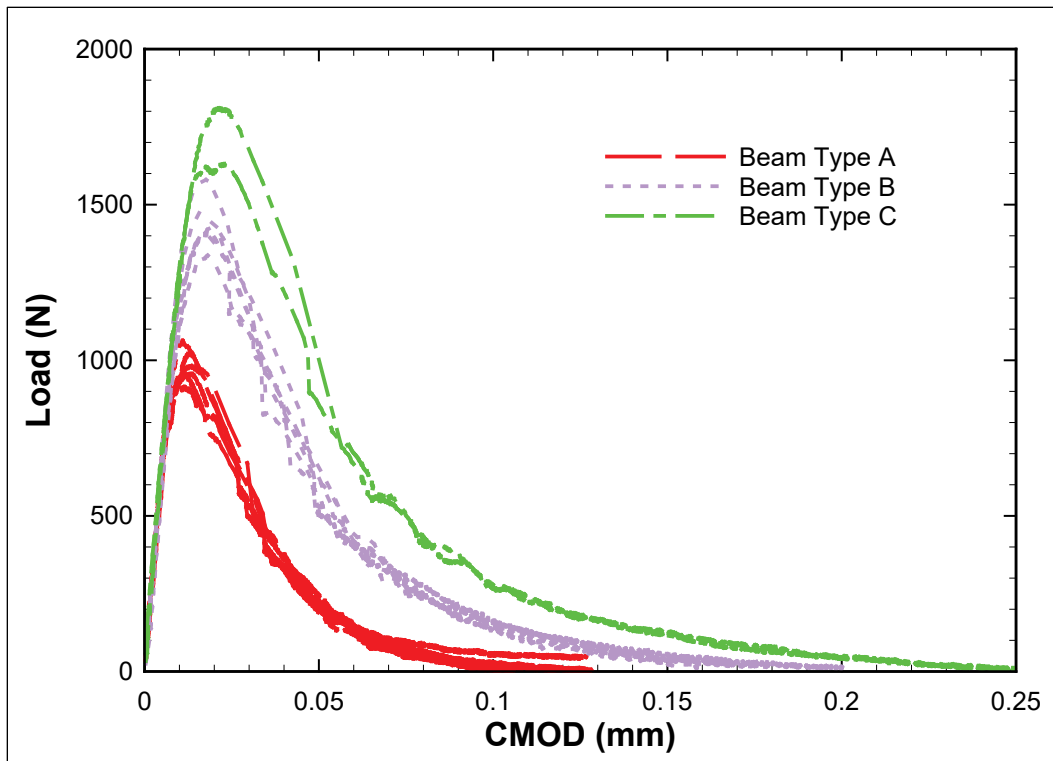


Table 2. Fracture energy for beam types A, B, and C.

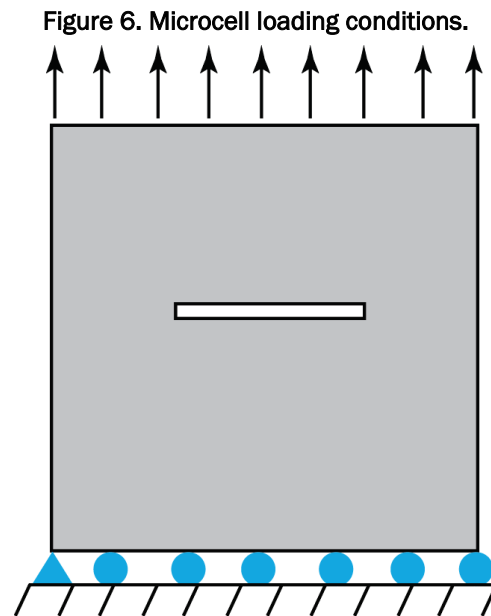
Beam Type	Test Number	Fracture Energy (N/m)
A	1	36.8
A	2	33.0
A	3	34.4
A	4	32.6
A	5	35.4
A	6	34.0
A	7	34.4
B	1	36.9
B	2	36.7
B	3	34.4
B	4	37.8
B	5	33.8
B	6	35.8
C	1	35.4
C	2	34.2
	Average =	35.0

4 Numerical Calculations

The experimental data can now be used to produce a damage evolution law that is informed by microscale calculations. The MIDM damage evolution law can then be implemented into the macroscale continuum code that will model the full-scale experiment to validate the process.

4.1 Microscale calculation

The microscale calculation was performed by using the two-dimensional static RKPM-based code known as the micro-nonlinear meshfree analysis program (NMAP-Micro), which was developed by UCSD-UCLA and the ERDC. The code was developed for microcrack informed multiscale modeling and is largely based on the work by Ren et al. (2011) and Lin et al. (2016). The microcell calculation setup for this study is shown in Figure 6. The dimensions of the microcell are 1.5 mm by 1.5 mm. The microcell is loaded in tension with a pre-existing crack in the center with a length of 0.15 mm, which is 10% of the microcell length. The microcell discretization is 101 by 101 particles for a total of 10,201 particles. The microcell upper surface displacement was incrementally loaded up to a vertical displacement of 0.1 mm. This microcell initial microstructure is a simplified microscopic scenario that is appropriate for a mode I fracture. Future work will include a more physical microstructural representation.



The constitutive response for the material in NMAP-Micro is a linear elastic material with a linear cohesive law. The form of the cohesive law implemented is shown in Figure 7. The material has an elastic response until it reaches a tensile strength threshold. Once over the tensile threshold, the material follows a linear softening down to a displacement, u_B , governed by the fracture energy (i.e., area of the triangle $u_A \sigma_T u_B$ in Figure 7). The required material parameters for the cohesive law and the values used for the UHPC considered in this study are listed in Table 3. The average fracture energy measured in the experiments was used for the microcell calculation.

Figure 7. Cohesive law implemented in NMAP-Micro.

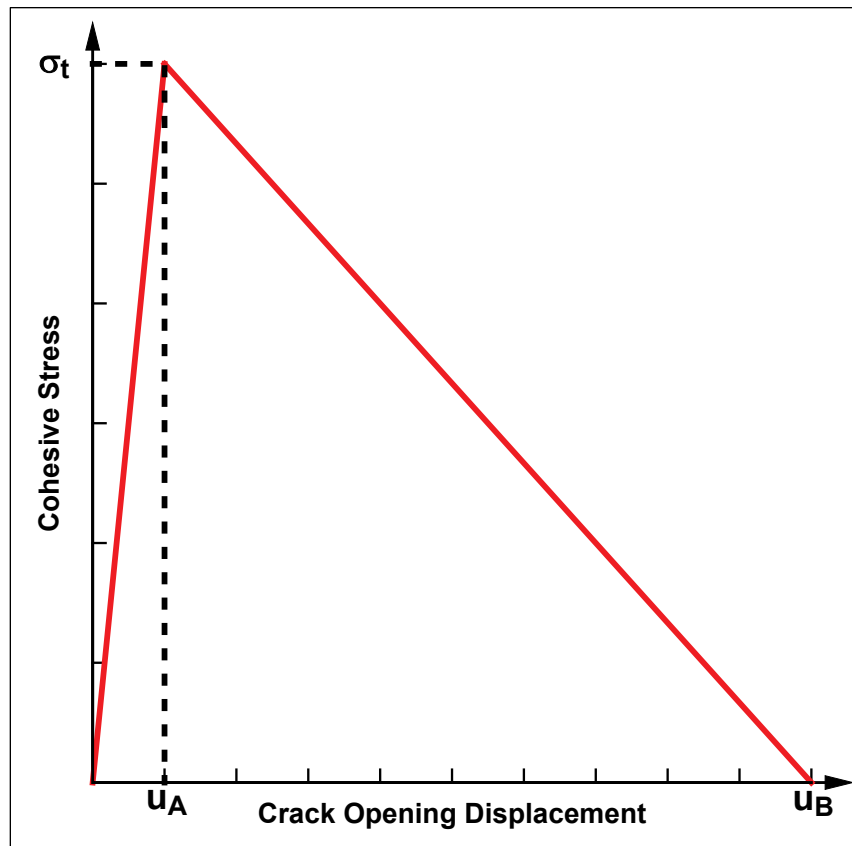
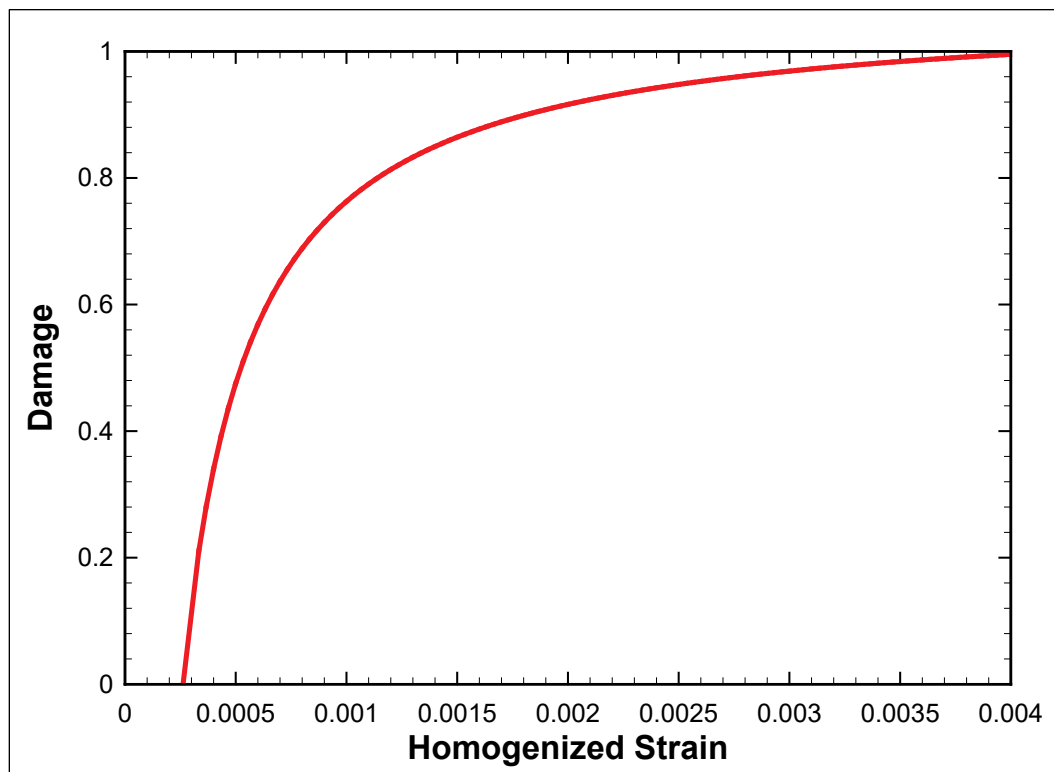


Table 3. Cohesive law parameters for microcell calculations.

Parameter	Value
Young's modulus (MPa)	44,300
Poisson's ratio	0.2
Tensile strength (MPa)	11.0
Fracture energy (N/m)	35.0

Once completed, the output of the microcell calculation is microscale-stresses and microscale-strains. These values must be processed through the energy-bridging homogenization described in Section 2.3 in order to produce a damage evolution function for use in the macroscale calculations. The resulting damage evolution function is shown in Figure 8. It should be noted that the microcell damage evolution function shown in Figure 8 is valid only for a macroscale particle spacing of 1.5 mm. If a different macroscale particle spacing is used along with this damage evolution curve, a well-known size effect would emerge. This can be eliminated by developing a scaling law that takes into account the proper size effect to reduce this mesh-sensitive behavior (Ren et al. 2011; Lin et al. 2016). In this study, only a macroscale particle spacing of 1.5 mm will be used to avoid the mesh-sensitive behavior.

Figure 8. Damage evolution curve based on the single-crack microscale calculation.

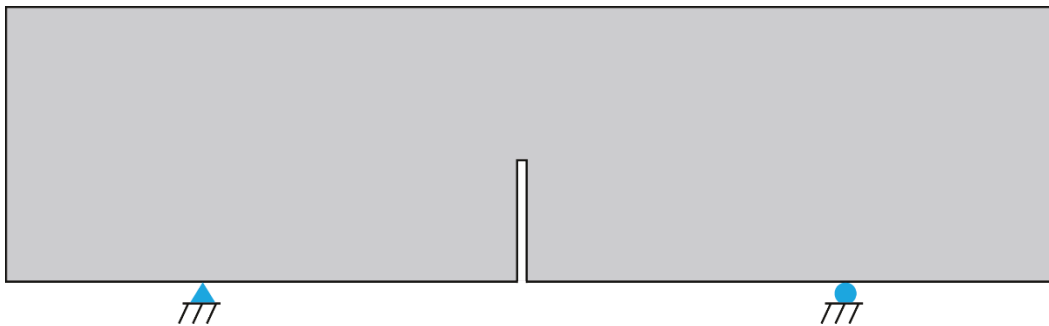


4.2 Macroscale calculation

The macroscale calculation was performed using the three-dimensional, explicit RKPM-based code known as nonlinear mesh-free analysis program (NMAP; Chi et al. 2012). NMAP was developed for the dynamic analysis of linear and nonlinear solid mechanics problems. The size of the three-point

bending beam problem in this study is small enough that an explicit code like NMAP can handle this type of problem. RKPM has shown great success in modeling quasi-static-type problems (Chen et al. 2002). The setup of the three-point bending calculation is shown in Figure 9. All three beam types were considered for the macroscale calculation. The dimensions are identical to the ones described in Table 1. The nodal spacing of the problem is exactly the microcell size of 1.5 mm in all directions. The top of the beam was loaded at a rate of 0.02 mm/s until the top displacement reached 0.2 mm of total displacement.

Figure 9. Three-point bending simulation setup.



The concrete constitutive model used in the macroscale calculation is the Advanced Fundamental Concrete (AFC) model developed by Adley et al. (2010). The AFC model is a three-invariant plasticity model that includes the effects of hydrostatic crushing, plastic flow, rate-dependency, and damage. The hydrostatic and deviatoric responses are decoupled for simplicity. The model was designed for modeling the dynamic response of concrete under high-rate loading conditions. A number of studies have shown that the AFC model can be applied to a large range of penetration type scenarios (Sherburn et al. 2014; Sherburn et al. 2015; Nordendale et al. 2016). The AFC model used in this study follows the approach of Sherburn et al. (2014) and Sherburn et al. (2015), which includes the MIDM tensile damage evolution function described in Section 4.1. This addition was not originally included in the AFC model of Adley et al. (2010). Although the AFC model was not primarily developed for quasi-static-type problems, it can be applied to this type of problem. A brief summary of the AFC model will now be described.

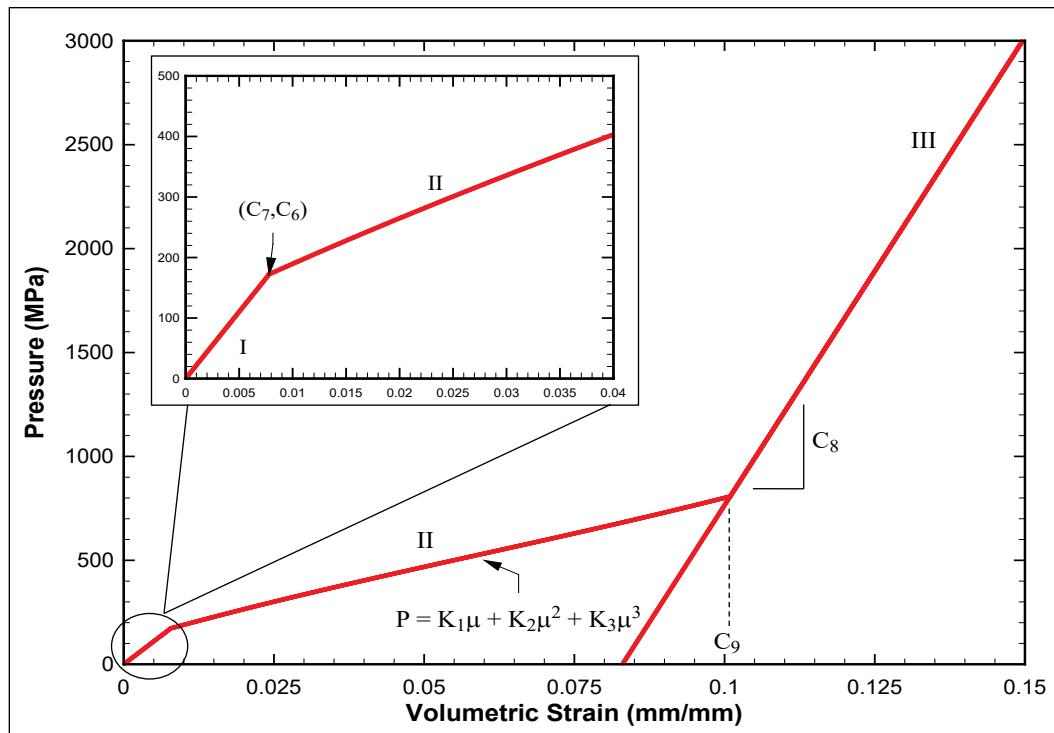
The hydrostatic response of the AFC model can be broken into three separate regimes, as shown in Figure 10. The first portion is regime I, where there is a linear bulk modulus hydrostatic response. The slope of the line is the initial bulk modulus of the material. Once the material reaches a

threshold point defined by the two parameters, C_6 and C_7 , the material enters regime II. Regime II is a nonlinear irreversible hydrostatic crushing portion that is defined by

$$P = K_1\mu + K_2\mu^2 + K_3\mu^3 \quad (19)$$

where K_1 , K_2 , and K_3 are input parameters, μ is the measure of volumetric strain defined by the ratio of the initial volume minus the current volume to the current volume, $(V_0 - V)/V$, and P is the pressure where compression is defined as positive. The third regime is defined by a locking bulk modulus, C_8 , and locking strain, C_9 . This point represents the point at which all the voids in the concrete have been crushed out of the concrete. The locking region is linear.

Figure 10. AFC hydrostatic fit for Cor-Tuf used in this study.



The AFC failure surface of the UHPC is described as the deviatoric response that is dependent on the pressure, strain rate, and damage. The failure surface in compression is described as

$$S_Y^{comp} = (C_1 - [C_2 + (C_1 - C_2)d^-]e^{-A_n P} + C_4 P)(1 + C_3 \ln(\dot{\epsilon}_n)), \quad (20)$$

where C_1, C_2, C_3, C_4 , and A_n are constants greater than zero; d^- is the compressive scalar damage term that goes from 0.0 to 1.0; and $\dot{\varepsilon}_n$ is a normalized strain rate. The normalized strain rate is defined by

$$\dot{\varepsilon}_n = \frac{\dot{\varepsilon}}{\dot{\varepsilon}_0}, \quad (21)$$

where $\dot{\varepsilon}_0$ is a reference strain rate. The reference strain rate is 0.0001 s⁻¹. The tensile failure surface is defined as

$$S_y^{tens} = (C_1 - [C_2 + (C_1 - C_2)d^-])(1 + C_3 \ln[\dot{\varepsilon}_n]) \frac{T_{max}(1-d^+)^P}{T_{max}(1-d^+)} \quad (22)$$

where T_{max} is the maximum allowable tensile pressure. The failure surface fit used in this study is shown in Figure 11. The compressive scalar damage, d^- , is defined by

$$d^- = \sum \left[\frac{\Delta\varepsilon_p}{PD_1} + \frac{\Delta\mu_p}{1.5C_0} \right], \quad (23)$$

where D_1 is a material constant, and $\Delta\varepsilon_p$ and $\Delta\mu_p$ are the plastic strain increment and volumetric strain increment, respectively. The three-invariant dependency of the AFC model is through calculation of the extension failure surface. First, the Lode angle is calculated, and a factor is calculated by using a Willam-Warnke Lode function (Fossum and Brannon 2006). The factor is then multiplied by the compressive failure surface to produce the extension failure surface. The AFC constants used in this study are shown in Table 4.

Figure 11. AFC failure surface fit for Cor-Tuf used in this study.

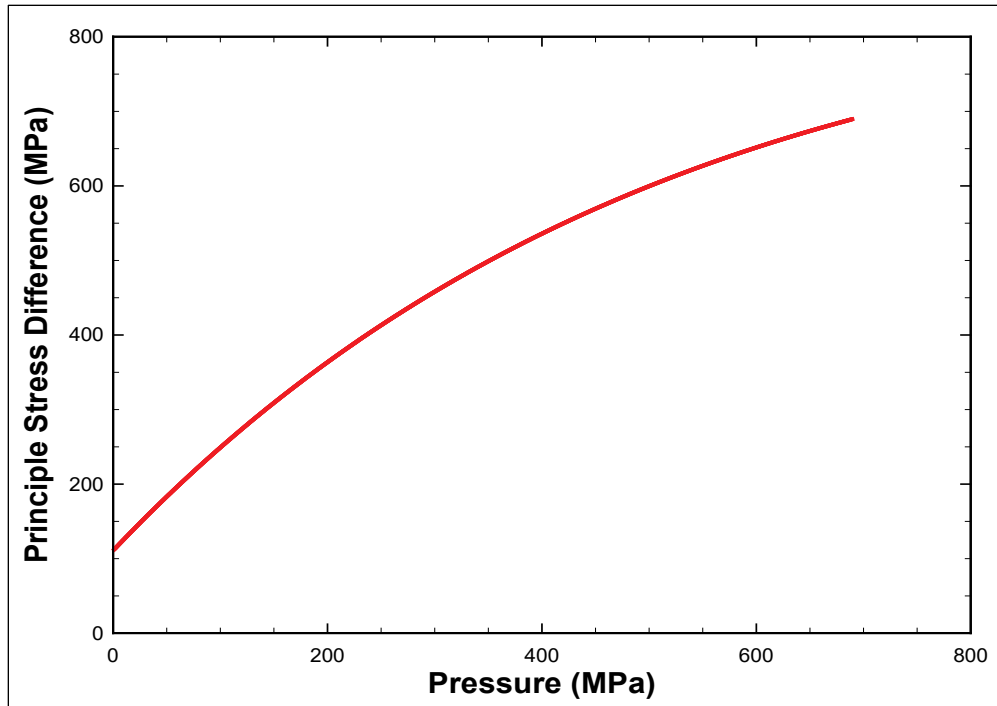


Table 4. AFC constants used for Cor-Tuf.

Parameter	Value
Density (kg/m ³)	2555.7
Shear Modulus (MPa)	18457
C ₁ (MPa) - Failure Surface Constant	1016.3
C ₂ (MPa) - Failure Surface Constant	942
C ₃ - Failure Surface Constant	0.003
C ₄ - Failure Surface Constant	0.10382
C ₅ (MPa) - Failure Surface Constant	792.88
C ₆ (MPa) - Pressure Where Crushing Begins	172.37
C ₇ - Volumetric Strain at Crushing	0.00781
C ₈ (MPa) - Locking Modulus	45039
C ₉ - Volumetric Strain at Locking	0.10094
K ₁ (MPa) - Hydrostatic Compression Constant	7919.2
K ₂ (MPa) - Hydrostatic Compression Constant	-29206
K ₃ (MPa) - Hydrostatic Compression Constant	187100
D ₁ (MPa ⁻¹) - Damage Constant	0.000406
A _N (MPa ⁻¹) - Failure Surface Constant	0.001735
T _{max} (MPa) - Maximum Allowable Tensile Pressure	6.89

The results of the NMAP macroscale calculations are shown in Figure 12. The NMAP calculations with the MIDM Cor-Tuf damage evolution function described in Section 4.2 generally match the trend of the experimental data across all three beam sizes. The peak stress of the NMAP calculations is on the high end of the beam type A and B and is overpredicted for beam type C. The softening portion of the beam test follows the general pattern; and when the fracture energy is calculated from these curves, the MIDM NMAP calculated fracture energy is within 2.6% of the average experimental fracture energy reported in Table 3 across all of the beam types. Figure 13 shows the tensile damage field contours for the MIDM NMAP three-point beam calculation. The tensile damage pattern in Figure 13 correctly mimics the expected single crack growth of the experimental beams. For an additional piece of comparison, the original AFC model response is included in Figure 14 to show how the damage evolution function presented in Section 4.1 is superior to the original AFC implementation for this type of problem. The original AFC model response predicts the fracture energy to be approximately 46% lower than the experimentally measured value. The original AFC model uses only Eq. 23 to calculate a single scalar damage that is purely phenomenological in nature. Since Eq. 23 has no concern for size effects, the softening response is not appropriately captured.

Figure 12. Experimental results compared to NMAP calculation.

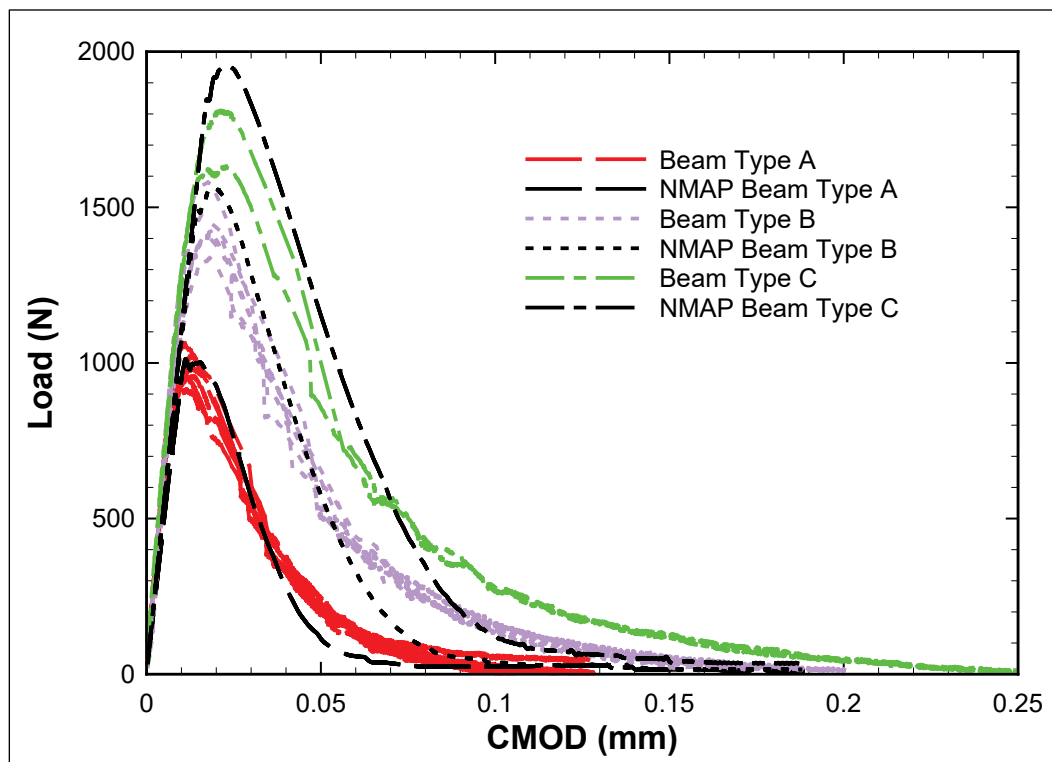


Figure 13. Damage field results of the NMAP MIDM three-point beam type A calculation.

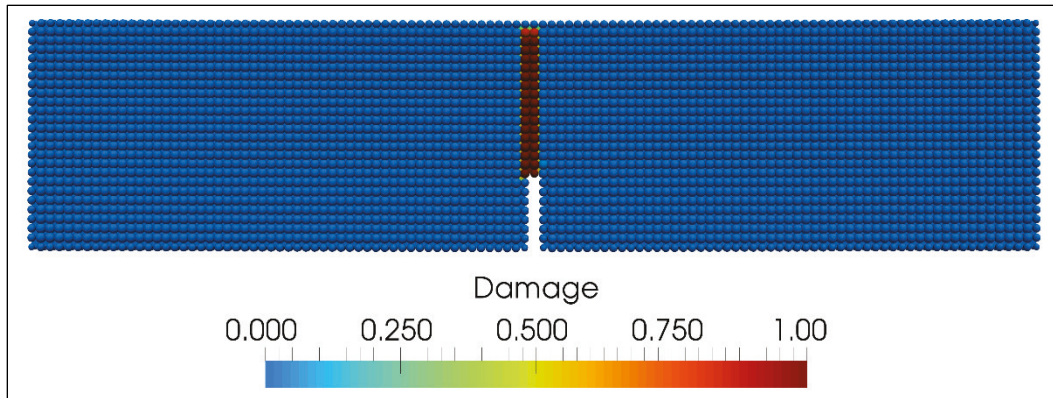
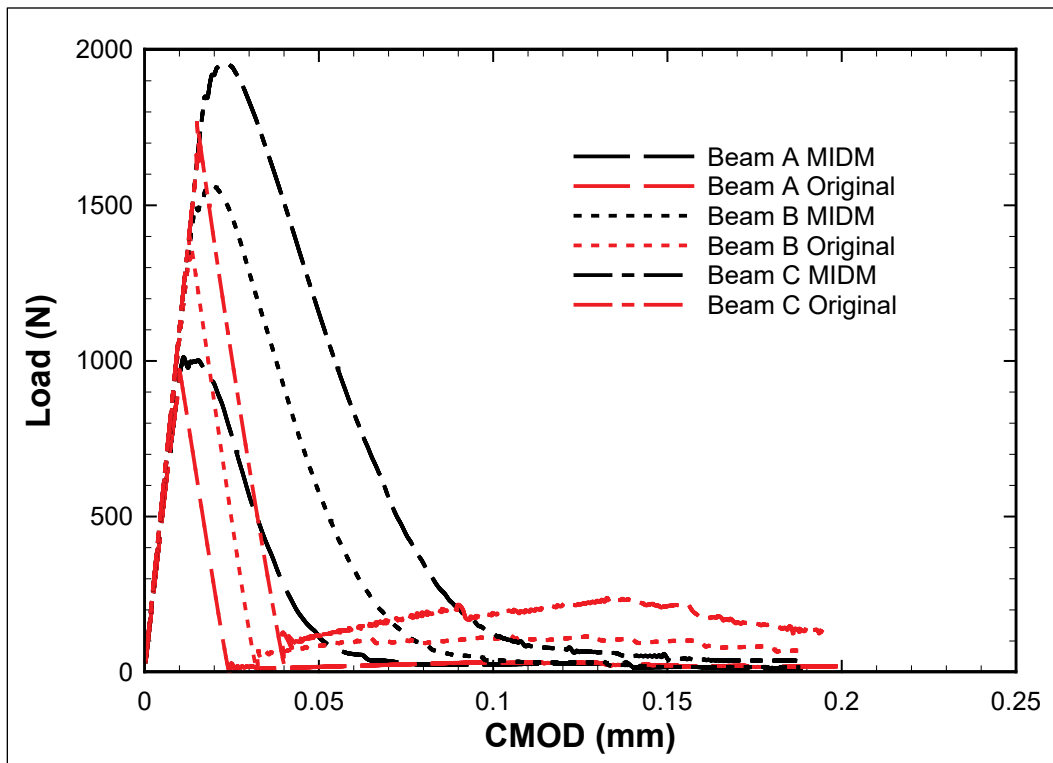


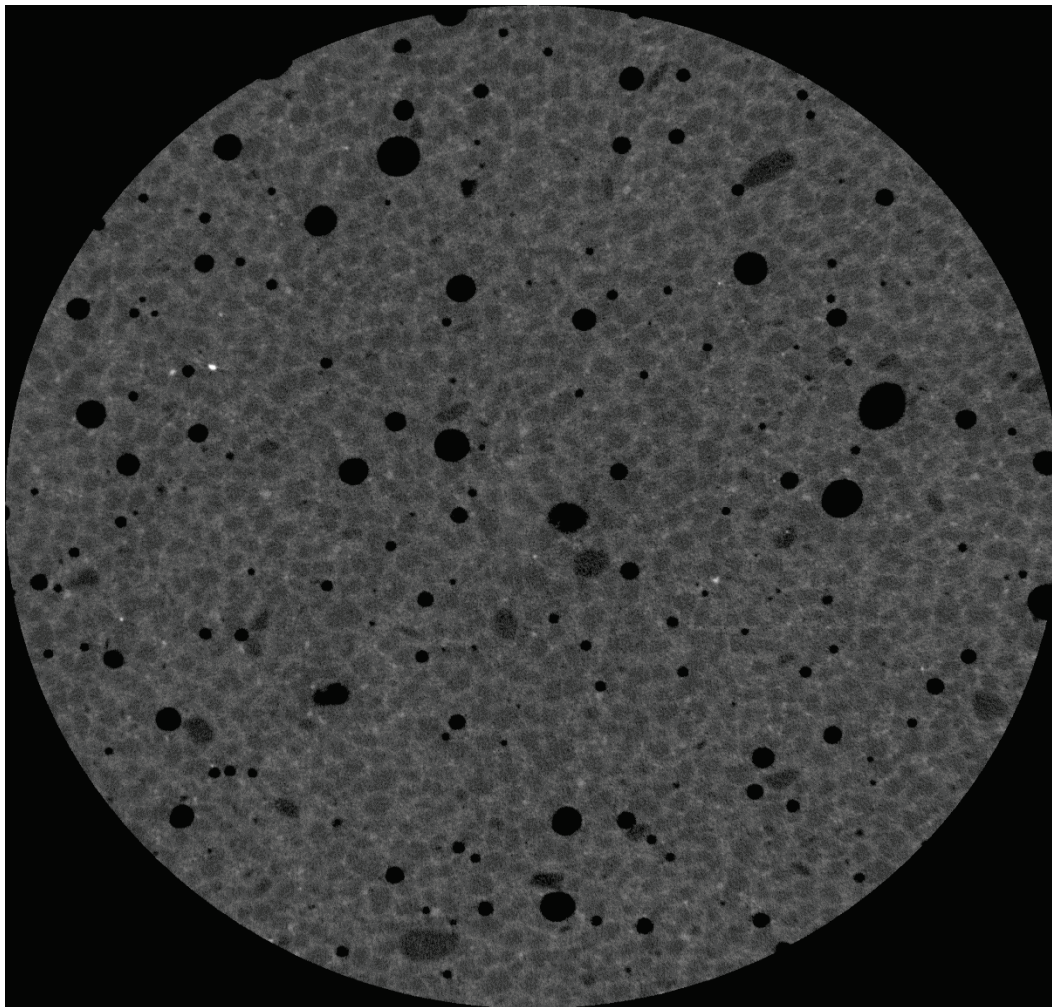
Figure 14. MIDM AFC NMAP calculations versus original AFC NMAP calculations.



One of the limitations of the MIDM approach in this study is that the damage evolution function in Figure 8 is applicable to a mode I type crack failure due to the simplified microstructure representation of the microscale calculations performed in this study. Ideally, the microscale calculation would contain all of the relevant microstructure features with appropriate properties.

Figure 15 shows an X-ray microcomputed tomography of the UHPC studied in this work. Future work will investigate incorporating a better representation of the microstructure into the microscale calculations in order to improve the applicability of the damage evolution function for this UHPC.

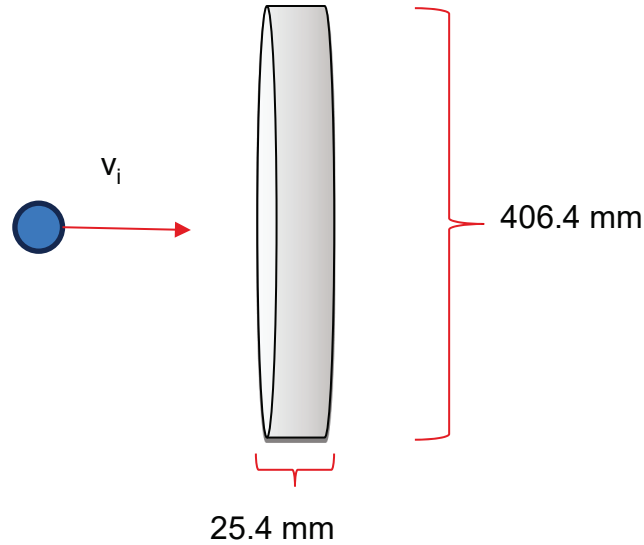
Figure 15. X-ray computed micro-tomography image of Cor-Tuf.



4.3 Ballistic numerical application

A dynamic application of the MIDM damage evolution law is a numerical ballistic perforation. The setup of the example ballistic perforation is a 12.7-mm-diameter steel projectile impacting a Cor-Tuf cylinder. The Cor-Tuf cylinder has a diameter of 406.4 mm and a thickness of 25.4 mm. A range of steel sphere impact velocity calculations was completed to show the perforation response of the target. The velocity range was between 300 m/s and 900 m/s. The basic setup of the numerical experiment is shown in Figure 16.

Figure 16. Setup of numerical ballistic perforation experiment.

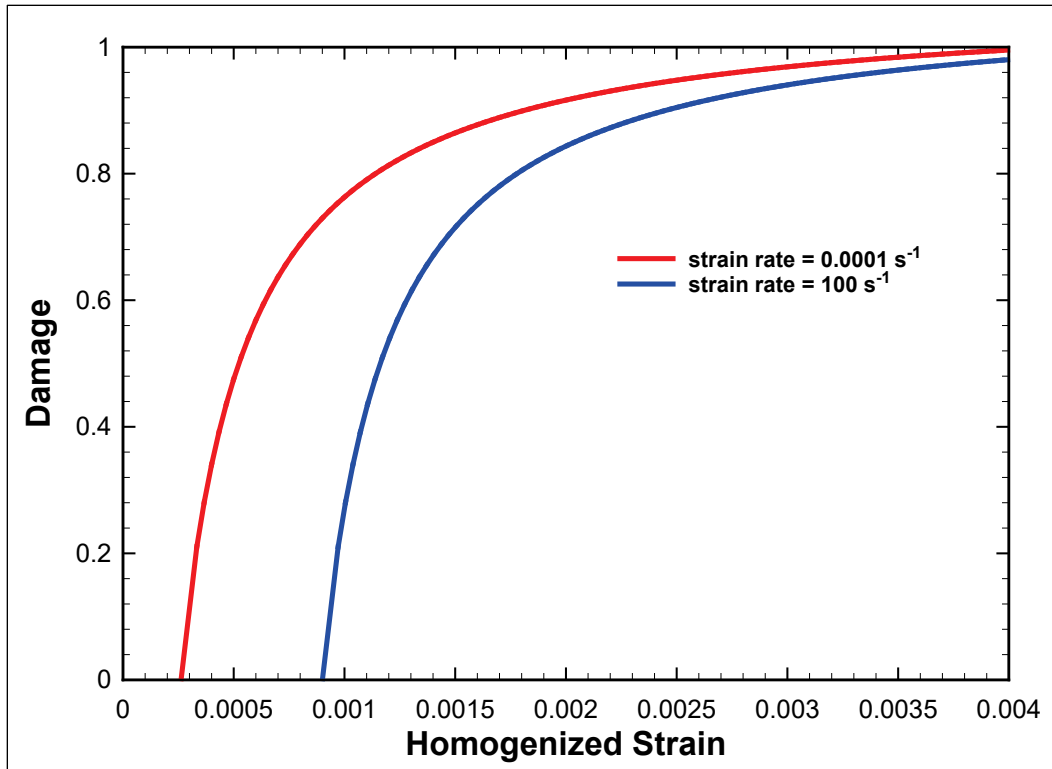


The MIDM damage evolution law shown in Figure 8 is valid for quasi-static situations. In order to accurately represent dynamic tension, some modifications to the damage evolution law must occur. It is well known in the literature that concrete has an increase in strength under dynamic loading (Hughes et al. 1993). This dynamic increase factor (DIF) is different based on whether concrete is loaded under a tension or a compression stress state. The DIF for compression is taken care of in the AFC by the parameter C_3 . The tension DIF will use a simple modification to the damage evolution law by shifting the damage evolution law based on the tensile strain rate and is defined as

$$\sigma_d = \sigma_s [1 + C_T \ln(\dot{\epsilon}_n)], \quad (24)$$

where σ_d and σ_s are the dynamic tensile stress and static tensile stress, respectively. The constant, C_T , controls the amount of dynamic strength increase. In this study, a value of C_T was chosen to be 0.186. The strain rate adjusted damage evolution law due to strain rate is shown in Figure 17.

Figure 17. Strain rate adjusted damage evolution law for two different strain rates.



The strain rate adjusted damage evolution law (Equation 24) was implemented into NMAP. The nodal spacing of the target and projectile was approximately 1.5 mm, which ensures the same spacing as the beam calculation and the microcell considered in Section 4.1. The steel sphere is treated as a rigid projectile and has a density of 7,850 kg/m³. The steel sphere contains 24,064 particles, and the Cor-Tuf target contains 1,285,233 particles. The range of residual velocity results of the NMAP calculations are shown in Figure 18. Based on inspection of Figure 18, the perforation limit velocity prediction is between 350 m/s and 400 m/s. The damage field plot for the 500-m/s calculation is shown in Figure 19. For comparison, an NMAP calculation was performed with the original AFC model and a 500-m/s impact velocity. The damage contours for this calculation are shown in Figure 20.

Figure 18. Residual velocity results of NMAP perforation calculations.

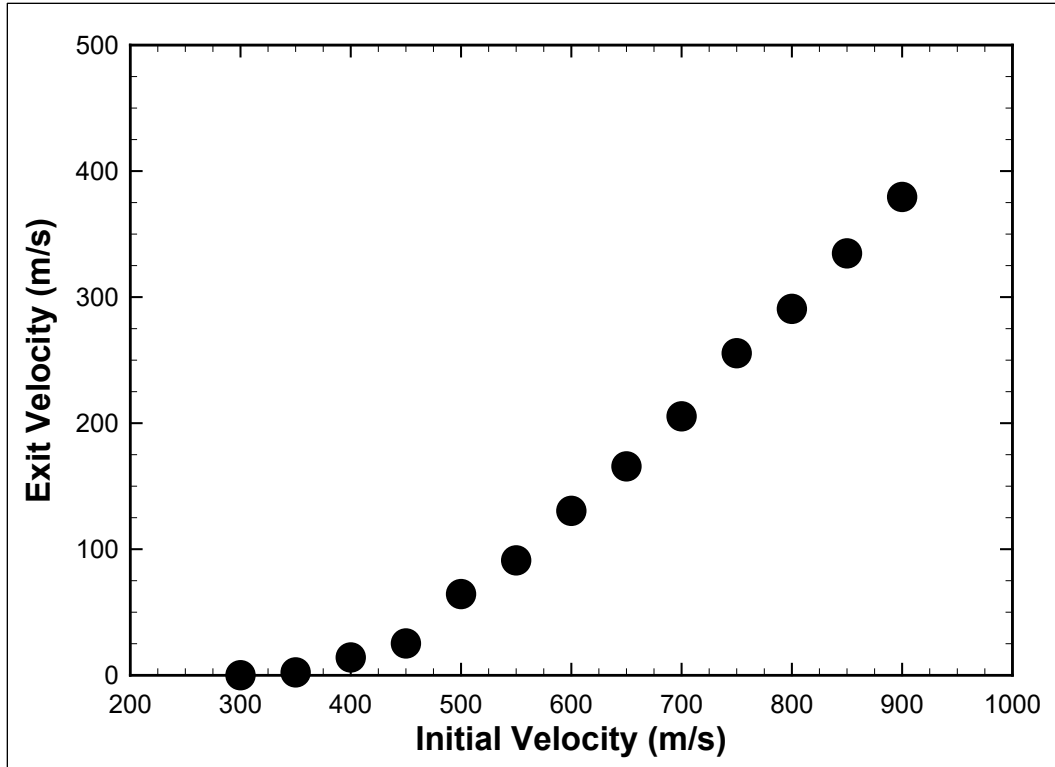


Figure 19. Damage field contours of the 500 m/s NMAP perforation calculation with MIDM improvements (impact face, back face, and side view).

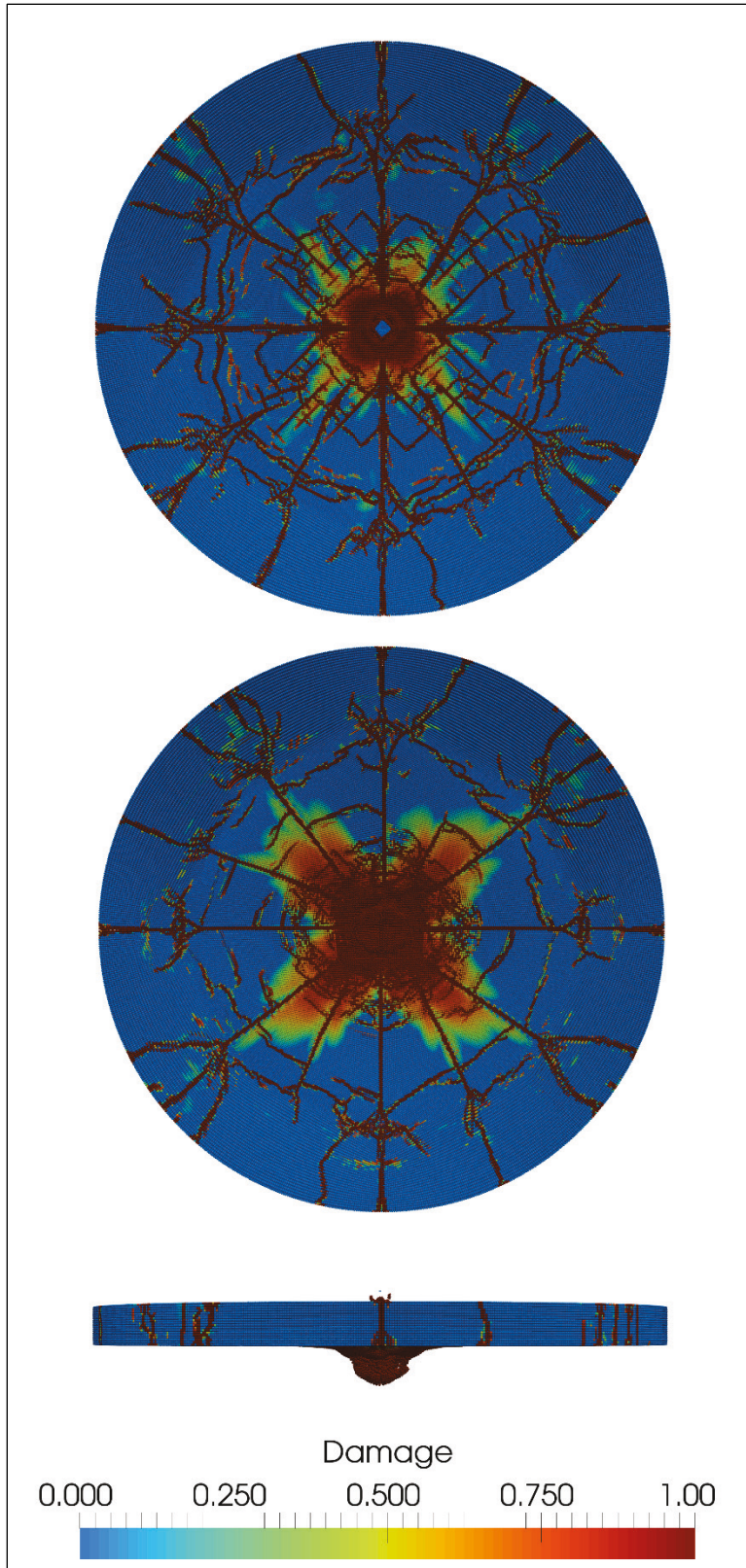
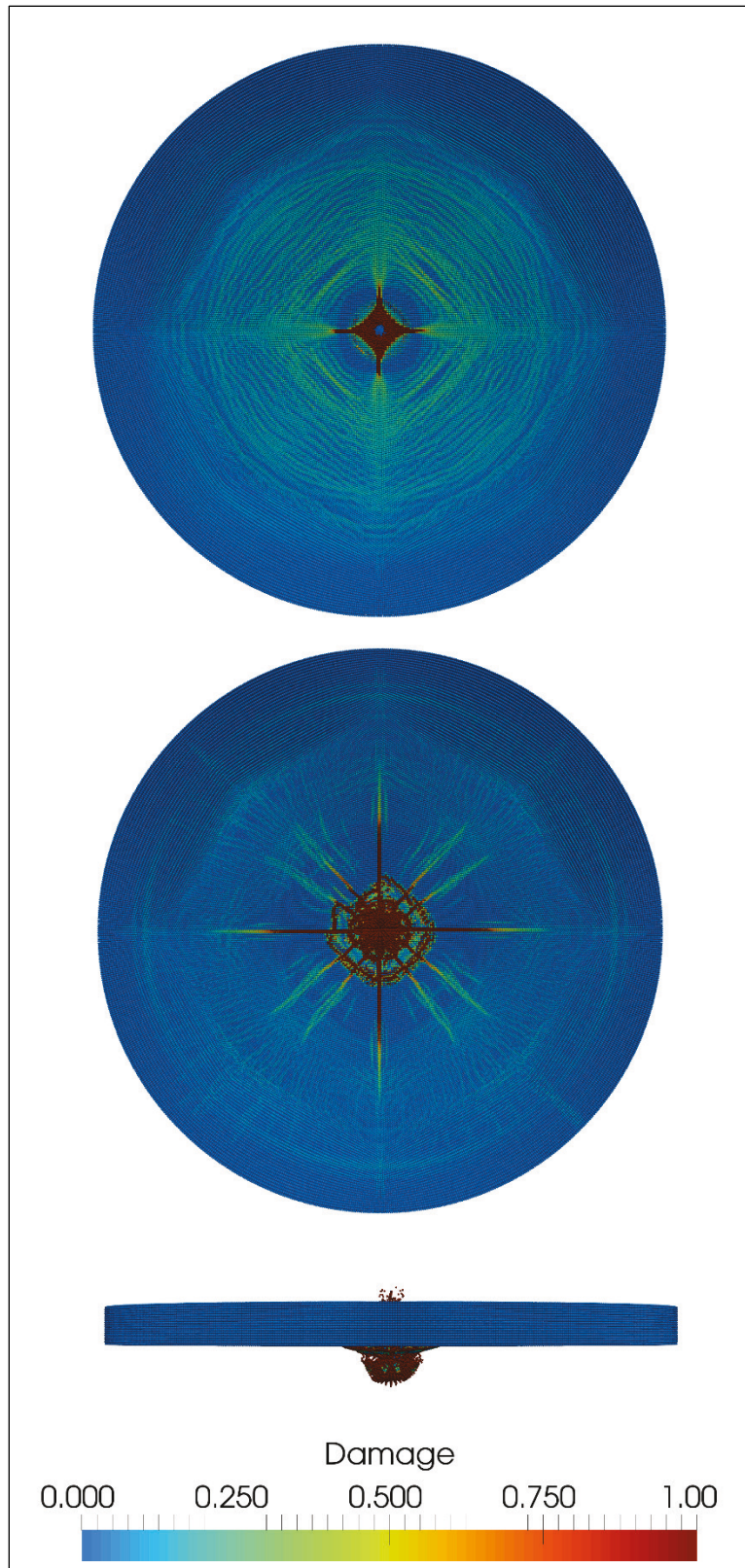


Figure 20. Damage field contours of the 500-m/s NMAP perforation calculation with original AFC model (impact face, back face, and side view).



The MIDM NMAP perforation calculation reveals that the newly implemented damage evolution law produces radial and circumferential tensile damage patterns on both the impact face and the back face. These patterns were expected for this type of perforation event. A clear difference between the original AFC model and the MIDM AFC model can be seen between the damage contours from all the different views in Figure 19 and Figure 20. In the original AFC model, the fully damaged material is seen only in a small localized area around the penetration impact area. The exit velocity of the MIDM AFC calculation was 61.0 m/s, and the analogous original AFC version was 63.9 m/s. From this comparison, exit velocity seems not to be sensitive to the tensile improvements.

5 Conclusions

The MIDM framework was applied to Cor-Tuf with corresponding physical experiments to inform the simplified microscale calculations. This represents the first time the experiments, microscale calculations, and macroscale calculations were completed entirely in one study. The damage evolution relationship produced through the MIDM framework has shown to be superior to the simple phenomenological damage function of the original AFC model and matches the experimentally measured results well.

A slight variation to the MIDM damage evolution law was introduced to account for the expected tensile DIF observed in experimental literature. The new dynamic MIDM damage evolution law was applied to a range of impact velocities on a cylindrical target to show the residual velocities for a range of impact velocities. The largest effect of the new dynamic MIDM damage evolution law was the distribution of damage, which is much more pronounced than it was in the original AFC model.

This study focused on a simple microscale approximation to show the utility of using the MIDM approach for application to Cor-Tuf when the correct material properties like fracture energy are included. Future work will concentrate on including realistic void distributions in the microscale calculations along with including the size effect with application to ballistic perforation experiments.

References

- Adley, M., A. Frank, K. Danielson, S. Akers, and J. O'Daniel. 2010. *The advanced fundamental concrete (AFC) model*. ERDC/GSL TR-10-51. Vicksburg, MS: U.S. Army Engineer Research and Development Center.
- Belytschko, T., Y. Krongauz, J. Dolbow, and C. Gerlach. 1998. On the completeness of meshfree particle methods. *International Journal of Numerical Methods In Engineering* 43(5):785-819.
- Chen, J. S., C. Pan, C. T. Wu, and W. K. Liu. 1996. Reproducing kernel particle method for large deformation analysis of non-linear structures. *Computational Methods in Applied Mechanics* 139(1-4):195-227.
- Chen, J. S., C. T. Wu, S. Yoon, and Y. You. 2001. A stabilized conforming nodal integration for Galerkin mesh-free methods. *International Journal of Numerical Methods in Engineering* 50(2):435-466.
- Chen, J. S., S. Yoon, and C. T. Wu. 2002. Nonlinear version of stabilized conforming nodal integration for Galerkin meshfree methods. *International Journal of Numerical Methods in Engineering* 53:2587-2615.
- Chi, S. W., C. H. Lee, J. S. Chen, M. J. Roth, and T. R. Slawson. 2012. *User's manual for non-linear meshfree analysis program (NMAP), version 1.0*. ERDC/GSL TR-12-36. Vicksburg, MS: U.S. Army Engineer Research and Development Center.
- Fossum, A. F., and R. M. Brannon. 2006. On a viscoplastic model for rocks with mechanism-dependent characteristic times. *Acta Geotechnica* 1(2):89-106.
- Guan, P. C., S. W. Chi, J. S. Chen, T. R. Slawson, and M. J. Roth. 2011. Semi-Lagrangian reproducing kernel particle method for fragment-impact problems. *International Journal of Impact Engineering* 38(12):1033-1047.
- Hughes, M. L., J. W. Tedesco, and C. A. Ross. 1993. Numerical analysis of high strain rate splitting-tensile tests. *Computers and Structures* 47(4/5):653-671.
- Jain, J. R., and S. Ghosh. 2009. Damage evolution in composites with a homogenization-based continuum damage mechanics model. *International Journal of Damage Mechanics* 18:533-568.
- Jenq, Y. J., and S. P. Shah. 1985. Two parameter fracture model for concrete. *ASCE Journal of Engineering Mechanics* 111(10):1227-41.
- Kachanov, L. M. 1958. Time of rupture process under creep conditions. *Izvestia Akademii Nauk USSR* 22(8):26-31.
- Lee, K., S. Moorthy, and S. Ghosh. 1999. Multiple scale computational model for damage in composite materials. *Computational Methods in Applied Mechanics* 172:175-201.

- Lin, S. P. 2014. A computational framework for the development of a stochastic micro-cracks informed damage model. PhD diss., University of California at Los Angeles.
- Lin, S. P., J. S. Chen, and S. Liang. 2016. A damage analysis for brittle materials using stochastic microstructural information. *Computational Mechanics* 57(3):371-385.
- Navalurkar, R. K., C. T. Hsu, S. K. Kim, and M. Wecharatana. 1999. True fracture energy of concrete. *ACI Materials Journal* 96(2):213-225.
- Nordendale, N. A., W. F. Heard, J. A. Sherburn, and P. K. Basu. 2016. A comparison of finite element analysis to smooth particle hydrodynamics for application to projectile impact on cementitious material. *Computational Particle Mechanics* 3(1):53-68.
- O'Neil, E. F. 2008. On engineering the microstructure of high-performance concretes to improve strength, rheology, toughness, and fragility. PhD diss., Northwestern University.
- Oskay, C., and J. Fish. 2007. Eigendeformation-based reduced order homogenization for failure analysis of heterogeneous materials. *Computational Methods in Applied Mechanics* 196:1216-1243.
- Rabotnov, Y. N. 1969. *Creep problems in structural members*. Amsterdam: North-Holland Publishing Company.
- Ren, X., J. S. Chen, J. Li, T. R. Slawson, and M. J. Roth. 2011. Micro-cracks informed damage models for brittle solids. *International Journal of Solids and Structures* 48:1560-1571.
- Sherburn, J. A., M. I. Hammons, and M. J. Roth. 2014. Modeling finite thickness slab perforation using a coupled Eulerian-Lagrangian approach. *International Journal of Solids and Structures* 51:4406-4413.
- Sherburn, J. A., M. J. Roth, J. S. Chen, and M. Hillman. 2015. Meshfree modeling of concrete slab perforation using a reproducing kernel particle impact and penetration formulation. *International Journal of Impact Engineering* 86:96-110.
- Sparks, P. A., and C. Oskay. 2016. The method of failure paths for reduced-order computational homogenization. *International Journal for Multiscale Computational Engineering* 14(5):515-534.
- Sutton, M. A., J. J. Orteu, and H. W. Schreier. 2009. *Image correlation for shape, motion and deformation measurements: Basic concepts, theory and applications*. The Netherlands: Springer.
- Williams, E. M., S. S. Graham, P. A. Reed, and T. S. Rushing. 2009. *Laboratory characterization of Cor-Tuf concrete with and without steel fibers*. ERDC/GSL TR-09-22. Vicksburg, MS: U.S. Army Engineer Research and Development Center.

REPORT DOCUMENTATION PAGE

Form Approved
OMB No. 0704-0188

Public reporting burden for this collection of information is estimated to average 1 hour per response, including the time for reviewing instructions, searching existing data sources, gathering and maintaining the data needed, and completing and reviewing this collection of information. Send comments regarding this burden estimate or any other aspect of this collection of information, including suggestions for reducing this burden to Department of Defense, Washington Headquarters Services, Directorate for Information Operations and Reports (0704-0188), 1215 Jefferson Davis Highway, Suite 1204, Arlington, VA 22202-4302. Respondents should be aware that notwithstanding any other provision of law, no person shall be subject to any penalty for failing to comply with a collection of information if it does not display a currently valid OMB control number. **PLEASE DO NOT RETURN YOUR FORM TO THE ABOVE ADDRESS.**

1. REPORT DATE (DD-MM-YYYY) April 2019		2. REPORT TYPE Final		3. DATES COVERED (From - To)	
4. TITLE AND SUBTITLE A Multiscale Meshfree Approach to Modeling Damage of Cor-Tuf without Fibers Using Fracture Energy Experiments				5a. CONTRACT NUMBER	
				5b. GRANT NUMBER	
				5c. PROGRAM ELEMENT NUMBER 61102	
6. AUTHOR(S) Jesse A. Sherburn, William F. Heard, Brett A. Williams, and Paul A. Sparks				5d. PROJECT NUMBER	
				5e. TASK NUMBER	
				5f. WORK UNIT NUMBER	
7. PERFORMING ORGANIZATION NAME(S) AND ADDRESS(ES) Geotechnical and Structures Laboratory U.S. Army Engineer Research and Development Center 3909 Halls Ferry Road Vicksburg, MS 39180-6199				8. PERFORMING ORGANIZATION REPORT NUMBER ERDC/GSL TR-19-12	
9. SPONSORING / MONITORING AGENCY NAME(S) AND ADDRESS(ES) U.S. Army Engineer Research and Development Center 3909 Halls Ferry Road Vicksburg, MS 39180-6199				10. SPONSOR/MONITOR'S ACRONYM(S) ERDC	
				11. SPONSOR/MONITOR'S REPORT NUMBER(S)	
12. DISTRIBUTION / AVAILABILITY STATEMENT Approved for public release; distribution is unlimited.					
13. SUPPLEMENTARY NOTES					
14. ABSTRACT Many continuum damage mechanics models for cementitious materials are typically phenomenological in design. Recent work has shown that a physics-based multiscale approach to modeling damage is efficient and effective. In order to use a multiscale approach, appropriate experimental data are necessary to model the microscale calculations that will then inform the continuum-scale calculations. This work uses the multiscale approach and experimentally determines the parameters necessary to model the microscale calculations. Notched three-point beam experiments were performed to determine the fracture energy of the ultra-high performance concrete known as Cor-Tuf. The fracture energy is then used by a simplified microscale calculation to determine a physics-based damage evolution equation that can be used in continuum-scale calculations. A meshfree method is used to show the usefulness of the newly determined damage evolution equation. Both a quasi-static application and a dynamic application are shown as examples.					
15. SUBJECT TERMS High strength concrete Continuum damage mechanics Multiscale modeling		Multiscale modeling Ultra-high-performance concrete Reproducing Kernel particle method		Constitutive modeling Fracture energy experiments Fracture mechanics	
16. SECURITY CLASSIFICATION OF:			17. LIMITATION OF ABSTRACT	18. NUMBER OF PAGES	19a. NAME OF RESPONSIBLE PERSON
a. REPORT Unclassified	b. ABSTRACT Unclassified	c. THIS PAGE Unclassified			39